# Aeroservoelastic Modeling and Robust Control for Gust Load Alleviation of an Experimental Wing

Felix Stalla*, Thiemo Kier†, and Gertjan Looye‡
*German Aerospace Center (DLR), 82234 Weßling, Germany*

Manuel Pusch§
*Munich University of Applied Sciences, 80335 Munich, Germany*

**Active gust load alleviation is a promising technique to reduce the structural weight of flexible transport aircraft wings with high aspect ratio, ensuring lower fuel consumption and environmental impact. The challenge is to develop a controller that is not only performant, but also robust, since the aircraft's environment cannot fully be captured within a computational model. Robust control is well suited to address this challenge by including uncertainties within the controller design. This paper describes using $\mu$-synthesis to develop a gust load alleviation controller for a flexible wing, to be tested in a wind tunnel experiment. The wing features both sweep and high aspect ratio. Five trailing edge control surfaces are installed for active load alleviation. Distributed acceleration sensors provide measurements for feedback control. The paper details the entire controller development, starting with the creation of an aeroservoelastic plant, using the Loewner framework as a novel addition to model the gust disturbance. After controller synthesis, the designed controller is validated in a nonlinear simulation, constituting a virtual representation of the wind tunnel experiment.**

## I. Introduction

Next generation transport aircraft will likely see wings with a high aspect ratio, as this allows to reduce induced drag and thereby increase efficiency [1]. If optimized for weight, these wings will exhibit a high flexibility, the aero-structural interaction will be more emphasized and the susceptibility to loads from maneuvers and gusts will be increased. To reduce these loads, active control technologies are promising. It has been shown that weight savings of up to 30% resulting in fuel savings of up to 10% can be achieved by implementing combined maneuver load alleviation (MLA) and gust load alleviation (GLA) functionalities [2, 3].

Load alleviation functions have already been successfully implemented on aircraft, as outlined in Ref. [4, 5]. These techniques however are primarily passive, not making full use of the possibilities opened up by advancements in automatic control technology. Applying such secondary flight control functions to high aspect ratio wings is a novelty and expected to yield larger effects compared to the application on conventional wings. To mature active MLA and GLA for high aspect ratio wings, experiments are indispensable. Wind tunnel and flight tests are part of the ongoing research activities [6, 7]. Different synthesis methods for load alleviation control are currently investigated. In Ref. [8], incremental nonlinear dynamic inversion is used, while robust control is applied for example in Ref. [9]. Another approach is to use an $H_2$-optimal blending, as detailed in [10]. When feedforward information is available, model predictive control presents another promising approach [11].

In this paper robust control is used to develop a feedback GLA controller to be tested in a wind tunnel experiment. Robust control has the advantage that uncertainties inevitably occurring in the model used for controller design can be accounted for in the synthesis itself. It allows to balance performance and stability requirements in the process. Since the developed controller will be tested in a wind tunnel experiment, this is of special importance.

The wind tunnel test campaign is conducted within the optimally load-adaptive aircraft (oLAF) project¶ of the German Aerospace Center (DLR). The wind tunnel test continues the research conducted in previous projects at DLR, see Ref. [6]. A flexible wing model with high aspect ratio and sweep is developed [12], representing the wing of

*Research Associate, Institute of System Dynamics & Control, felix.stalla@dlr.de
†Research Associate, Institute of System Dynamics & Control, thiemo.kier@dlr.de, AIAA Member.
‡Department Head, Institute of System Dynamics & Control, gertjan.looye@dlr.de, AIAA Member.
§Professor, Department of Mechanical, Automotive and Aeronautical Engineering, manuel.pusch@hm.edu
¶See acknowledgments for further details on the DLR oLAF project.

a long-range transport aircraft. Five trailing edge control surfaces are installed for load alleviation, while spanwise distributed acceleration sensors capture the flexible motion due to atmospheric disturbances. A CAD representation of the oLAF wind tunnel model is shown in Fig. 1. A gust generator introduces disturbances into the air flow, exciting the flexible wing. By applying feedback control, the structural loads due to these disturbances shall be reduced. The experiment will be conducted at subsonic speeds, the freestream velocity being 50 m/s.

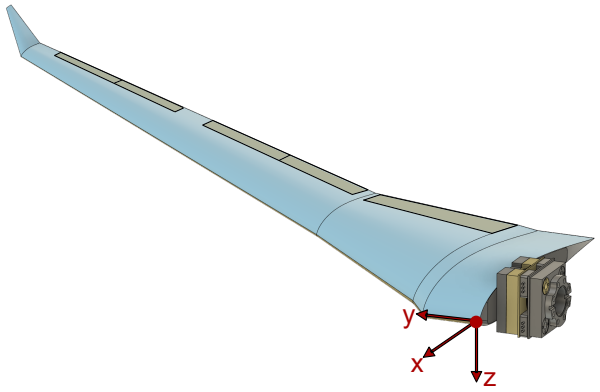


**Fig. 1 CAD model[‖] of the oLAF wind tunnel model**

This paper presents the model-based design of the GLA controller for the experimental flexible wing. As stated, the main challenge in designing a controller to be used in an experiment is to ensure sufficient robustness to unmodeled dynamics, changing operating conditions and neglected dynamics. Additionally, the high number of sensors and control surfaces is demanding, and best solved by an optimal control strategy. Thus, the GLA controller is designed using $\mu$-synthesis ($D$-$K$-iteration), an extension to $H_\infty$ robust optimal control [13]. Performance requirements are defined to reduce the integral loads at the wing-root (wing-root bending and torsion moment) induced by a gust. Robustness will be ensured by integrating structured multiplicative uncertainties at the plants input and output. $\mu$-synthesis has already been applied for GLA in Ref. [9], but within the present work the method is applied to a wind tunnel model using a wing with a high number of control surfaces and acceleration sensors.

The following not only details the controller design itself (Sections V and VI), but provides an overview of the steps necessary to obtain the GLA controller (Sections II through IV). The first step in model-based controller design is to derive a mathematical representation of the aeroservoelastic plant. The modeling process following Ref. [14] uses the VarLoads environment [15, 16]. The modeling involves structural dynamics, aerodynamic forces, aero-structural coupling, actuator dynamics and sensors. Next, the gust disturbance is added. Here, a novel aspect is the application of the Loewner framework [17], which allows to obtain a very precise gust model with a low number of states. The model components are assembled and two types of models are created: a nonlinear MATLAB-Simulink simulation, and a linear state-space model which is order reduced, to be suitable for $\mu$-synthesis. After the controller synthesis, a validation of the controller is performed within the nonlinear MATLAB-Simulink simulation, where both actuator saturation and delay are considered. The load-reduction potential and the robustness is examined in detail. The controller whose design is described here will be validated in the oLAF wind tunnel experiment in 2024.

## II. Aeroservoelastic Modeling of the Flexible Wing

The first necessary step to be able to perform model-based controller design is to derive a comprehensive aeroservoelastic model of the experimental flexible wing including gust disturbance. This model is developed throughout Sections II to IV. For those primarily interested in controller design, skip directly to Section V.

The theory of the modeling process is outlined in Ref. [14]. Baseline of the mathematical representation of the aeroservoelastic plant are the (nonlinear) equations of motion (EOM) based on mean axes [14, 18]:

$$\begin{aligned} \begin{bmatrix} m_b \cdot (\dot{\mathbf{V}}_b + \boldsymbol{\Omega}_b \times \mathbf{V}_b - \mathbf{T}_{bE} \cdot \mathbf{g}_E) \\ \mathbf{J}_b \cdot \dot{\boldsymbol{\Omega}}_b + \boldsymbol{\Omega}_b \times (\mathbf{J}_b \cdot \boldsymbol{\Omega}_b) \end{bmatrix} &= \boldsymbol{\Phi}_{gb}^T \cdot \mathbf{P}_g^{ext}, \\ \mathbf{M}_{ff} \cdot \ddot{\mathbf{u}}_f + \mathbf{B}_{ff} \cdot \dot{\mathbf{u}}_f + \mathbf{K}_{ff} \cdot \mathbf{u}_f &= \boldsymbol{\Phi}_{gf}^T \cdot \mathbf{P}_g^{ext}. \end{aligned} \tag{1}$$

[‖] CAD model supplied by DLR-AE-LAE. Point of contact: Johannes Dillinger, research associate, johannes.dillinger@dlr.de

The EOM are denoted in the modal domain, the notation is in accordance with the set definition (subscripts) in the Nastran Aeroelastic Analysis User's Guide [19]. The first equation expresses the rigid body motion ($b$-set), while the second expresses the flexible motion ($f$-set). The rigid body motion is described by six equations, using the linear velocity $\mathbf{V}_b$ and the rotational velocity $\mathbf{\Omega}_b$. The flexible motion is captured by the modal deflection $\mathbf{u}_f$, the number of equations depends on modal truncation. The structural properties are captured within the wing's mass $m_b$, its inertia tensor $\mathbf{J}_b$ and its modal matrices of mass $\mathbf{M}_{ff}$, damping $\mathbf{B}_{ff}$ and stiffness $\mathbf{K}_{ff}$. Gravity is taken into account by $\mathbf{g}_E$.

The excitation of rigid and flexible dynamics by external forces $\mathbf{P}_g^{ext}$ is given on the right hand side of the equation ($g$-set, structural set). These forces are created from aerodynamics and the gust disturbance. The eigenvector matrices $\mathbf{\Phi}_{gb}$ and $\mathbf{\Phi}_{gf}$ transfer the forces to the modal domain, these forces are commonly called generalized forces [18].

The aim of active GLA is to reduce the loads acting on the aircraft or wing in response to a gust disturbance. Thus it is important to recover the loads to quantify the effectiveness of the load alleviation measures. Here, the force summation method (FSM) [20] will be used (the loads from damping are generally small and can be neglected):

$$\begin{aligned} \mathbf{P}_g^{FSM} &= \mathbf{P}_g^{ext} - \mathbf{P}_g^{inertia} \\ &= \mathbf{P}_g^{ext} - \mathbf{M}_{gg} \cdot (\mathbf{\Phi}_{gb} \cdot \ddot{\mathbf{u}}_b + \mathbf{\Phi}_{gf} \cdot \ddot{\mathbf{u}}_f). \end{aligned} \tag{2}$$

In the following subsections, the different domains of modeling are presented, before the overall model is assembled in Section IV. Aim is to obtain a low order model with sufficient accuracy, as the order of the controller scales with the model order. The wind tunnel test is conduced at subsonic conditions with a Mach number of 0.15. The freestream velocity is 50 m/s, while sea level values from the standard atmosphere are used for pressure, density and temperature.

### A. Structural Modeling

The structural model is represented by the matrices on the left side of the flexible EOM in Eq. 1. The mass, damping and stiffness matrix are extracted from a finite element (FE) model[**]. To further simplify the structural model, a Guyan reduction (static condensation) [21] to a beam representation along the loads reference axis is performed. A modal truncation [22] reduces the order of the model further. 15 flexible modes were found to sufficiently represent the dynamic response. To reduce the loads induced by atmospheric disturbances like gusts, the primary target is to damp the lowest frequency flexible mode (first mode). In the undamped system without aerodynamic contribution this mode occurs at about 50 rad/s. Figure 2 displays the mode shape of the first four flexible mode shapes of lowest frequency.

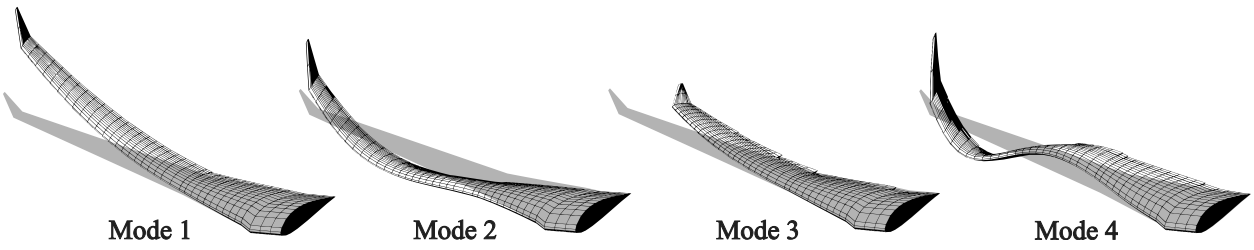


**Fig. 2 First four normal modes of the oLAF wind tunnel model**

A special feature of the modeling for a wind tunnel model is the rigid body motion (RBM). The model is not a free-flying aircraft. Instead, a pre-defined RBM is enforced. Here, only a motion in pitch will be considered. Using Eq. 1, the imposed rotation, velocity, and acceleration creates a load $\mathbf{P}_g^{ext}$ acting on the flexible EOM.

### B. Aerodynamic Modeling

The external forces on the right hand side of Eq. 1 stem from aerodynamics, as there are no propulsive forces acting on the wind tunnel model. Steady and unsteady generalized aerodynamic forces are calculated using the doublet lattice method (DLM) [23, 24]. This method is based on potential flow theory, using the unsteady Prandtl-Glauert equation [25]. For subsonic conditions at Mach 0.15, this method yields sufficiently accurate results. For the DLM, the wing is discretized into panels, as shown in Fig. 3a. Applying the DLM yields aerodynamic-influence-cofficient (AIC) matrices $\mathbf{Q}_{jj}$ in the frequency domain, linking the downwash $\mathbf{w}_j$ to the pressure coefficient $\mathbf{\Delta c}_{p,j}$ of each panel $j$. The AIC

[**]FE model supplied by DLR AE-LAE. Contact: Johannes Dillinger, research associate, johannes.dillinger@dlr.de.

matrices are calculated for multiple reduced frequencies $k$ [26] in the range of 0 to 4.5. Defining a pressure-to-load matrix $\mathbf{S}_{kj}$ and multiplying with the dynamic pressure $q_\infty$, the following forces result at the reference point ($k$-set) of each panel (careful not to confuse the reference point set, $k$ as an index, with the reduced frequency, $k$):

$$\mathbf{P}_k^{aero}(k) = q_\infty \cdot \mathbf{S}_{kj} \cdot \mathbf{Q}_{jj}(k) \cdot \mathbf{w}_j, \qquad k = \frac{\omega \cdot c_{ref}}{2 \cdot U_\infty}. \tag{3}$$

The downwash $\mathbf{w}_j$ is induced by the flexible motion of the wing, the rigid body motion, or the control surface deflection. This leads to a coupling between structural and aerodynamic model as described in the next section.

### C. Aero-Structural Coupling

From Eq. 1 and 3 it becomes clear that structural and aerodynamic model are interconnected, since displacements and forces in each model depend on the other model. To obtain the coupling, two methods are employed, to best capture the structural behavior of the wing: rigid body splines [27] and infinite-plate-spline-type radial basis functions [28]. Thereby it is ensured that the rigidity of the spars running in chordwise direction is correctly modeled. The two steps combined yields the splining matrix $\mathbf{T}_{kg}$, mapping displacements from structural grid points ($g$-set) to aerodynamic reference points ($k$-set). This matrix thus allows to calculate the orientation of the aerodynamic panels once the wing is deformed, while its transpose allows to obtain structural forces derived from aerodynamics.

Additionally, a mapping between control surface deflection ($x$-set) and orientation of the aerodynamic panels ($k$-set) is required. This mapping is purely geometric and is represented by the matrix $\mathbf{T}_{kx}$. The aerodynamic contribution to the external forces can now be stated by combining the splining matrix with Eq. 3, yielding:

$$\mathbf{P}_g^{aero}(k) = q_\infty \cdot \mathbf{T}_{kg}^T \cdot \mathbf{S}_{kj} \cdot \mathbf{Q}_{jj}(k) \cdot \mathbf{w}_j. \tag{4}$$

This equation is still defined in the frequency domain for a discrete reduced frequency $k$. The contribution to the downwash stems from the flexible motion ($f$-set), the rigid body motion ($b$-set) and the control surfaces ($x$-set):

$$\begin{aligned} \mathbf{w}_j = &\left(\mathbf{D}_{jk}^1 + i \cdot k \cdot \mathbf{D}_{jk}^2\right) \cdot \mathbf{T}_{kg} \cdot \mathbf{\Phi}_{gf} \cdot \mathbf{u}_f \\ + &\left(i \cdot k \cdot \mathbf{D}_{jk}^2\right) \cdot \mathbf{T}_{kg} \cdot \mathbf{\Phi}_{gb} \cdot \mathbf{u}_b \\ + &\left(\mathbf{D}_{jk}^1 + i \cdot k \cdot \mathbf{D}_{jk}^2\right) \cdot \mathbf{T}_{kx} \cdot \mathbf{u}_x. \end{aligned} \tag{5}$$

The only missing contribution in the external forces on the right hand side of Eq. 1 is the gust, which will be introduced in Section III, since the aerodynamic modeling will differ. Figure 3 presents the aeroservoelastic model with control surfaces (blue - wing, yellow - control surfaces). Aerodynamic panels for the DLM computation as well as the structural nodes (red) of the condensed model are shown in Fig. 3a.

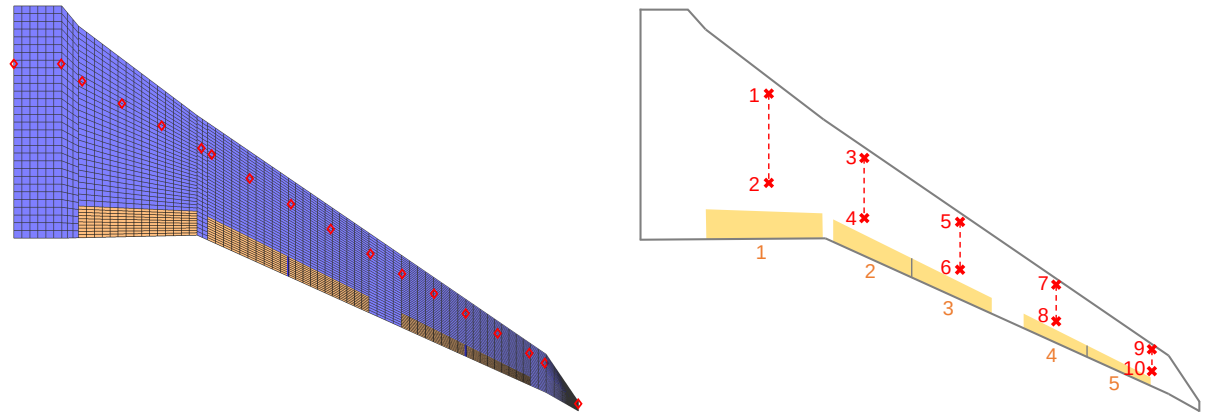


**(a) Aerodynamic discretization and structural nodes** **(b) Location and ID of control surfaces and sensors**

**Fig. 3 Aeroservoelastic model of the oLAF wind tunnel model**

### D. Rational Function Approximation

So far, the external forces due to aerodynamics (coupled with the structural motion) are only available in the frequency domain, at multiple reduced frequencies k. To conduct a time simulation or construct a state-space model for controller synthesis, the aerodynamic data needs to be available in the time domain. However, for the terms in Eq. 4 and 5 no suitable Laplace or Fourier transform is available. To convert the AIC matrices, an rational function approximation (RFA) is applied, to obtain terms which can be handled by a Laplace transform. Here, Roger's RFA [29, 30] is employed. As introduced in Ref. [14], a so-called physical RFA on the AIC matrix $\mathbf{Q}_{gj} = \mathbf{T}_{kg}^T \cdot \mathbf{S}_{kj} \cdot \mathbf{Q}_{jj}$ is used, to allow for separating steady and unsteady aerodynamic force. One obtains (note this is only one of multiple possible realizations of the RFA):

$$\mathbf{Q}_{gj}(ik) \approx \mathbf{Q}_{gj}^0 + \mathbf{Q}_{gj}^1 \cdot ik + \mathbf{D} \cdot \left( ik \cdot \mathbf{I}_{n_p \cdot n_q} - \mathbf{R} \right)^{-1} \cdot \mathbf{E} \cdot ik, \tag{6}$$

$$\mathbf{D} = \begin{bmatrix} \mathbf{Q}_{gj}^3 & \mathbf{Q}_{gj}^4 & \cdots & \mathbf{Q}_{gj}^{n_p+2} \end{bmatrix}, \qquad \mathbf{R} = \text{diag}\left( \begin{bmatrix} -p_1 \mathbf{I}_{n_j} & \cdots & -p_{n_p} \mathbf{I}_{n_j} \end{bmatrix} \right), \qquad \mathbf{E} = \begin{bmatrix} \mathbf{I}_{n_j} & \cdots & \mathbf{I}_{n_j} \end{bmatrix}^T. \tag{7}$$

The AIC matrix is split into multiple terms, the coefficients are determined by a least-squares fit [29]. The AIC matrix with subscript 0 captures the quasi-steady aerodynamic contribution, while the matrix with subscript 1 represents the added mass term. An acceleration matrix is not present when applying the physical RFA [14]. The last term including $\mathbf{D}$, $\mathbf{E}$ and $\mathbf{R}$ is used to capture so-called aerodynamic lag states, resulting from unsteady aerodynamics [22]. The poles $p_i$ used in this term must be specified. Here, a number of $n_p = 8$ poles are used. Laplace transforming the elements of the performed RFA in Eq. 7 and combining with Eq. 4 yields the time domain equivalent of the generalized aerodynamic forces, i.e. Eq. 4 transferred to the time domain [14]:

$$\begin{aligned} \mathbf{P}_g^{aero}(t) &= q_\infty \cdot \left( \mathbf{Q}_{gj}^0 \cdot \mathbf{w}_j \right) + q_\infty \left( \mathbf{Q}_{gj}^1 \cdot \left( \frac{c_{ref}/2}{U_\infty} \right) \cdot \dot{\mathbf{w}}_j + \mathbf{D} \cdot \mathbf{x}_L(\dot{\mathbf{w}}_j) \right), \\ \dot{\mathbf{x}}_L &= \mathbf{R} \cdot \left( \frac{U_\infty}{c_{ref}/2} \right) \cdot \mathbf{x}_L + \mathbf{E} \cdot \dot{\mathbf{w}}_j. \end{aligned} \tag{8}$$

In above's equation the vector $\mathbf{x}_L$ denotes the aerodynamic lag states [22]. The downwash $\mathbf{w}_j$ and its derivative supplied to the equation need to be calculated as presented in Eq. 5. In the time domain, the term $ik$ is equivalent to a (scaled) derivative of the respective motion. The scaling terms including the velocity $U_\infty$ and the reference chord $c_{ref}$ stem from the use of the reduced frequency $k$, see Eq. 3.

This concludes the modeling of the external forces stemming from a motion of the wing or its control surfaces. The last contribution to the right hand side of the EOM is the force from a gust, which will be detailed in Section III. The aero-structural model composed of Eq. 1 and 4 can be simulated.

### E. Actuator and Sensor Modeling

The control surface motion generates a downwash as described in Eq. 5. The control surfaces are moved by actuators. Due to physical limitations, a commanded deflection is not instantly achieved. These constraints are captured within an actuator model that will provide the current deflection, rate and acceleration of the control surface based on a commanded deflection. The actuator model is added to the aeroservoelastic plant. The electromechanical actuators of the oLAF wind tunnel model can be described by a first order linear time-invariant system. The model is based on characteristics of the actuators which were used in a previous experiment of DLR [31]. Besides the governing transfer function of the system, non-linearities have to be considered, as given for example in Ref. [32]. In accordance with Ref. [31], the roll-off of the actuators occurs at 90 rad/s, the limit on deflection is 10°, the rate limit 1129°/s, the acceleration limit 79540°/s$^2$ and the dead time 4.3 ms. All five control surfaces feature the same type of actuator.

Ten vertical acceleration sensors are distributed across the span of the wing to capture the motion and deliver signals for feedback control. Two sensors each are located at the same spanwise location, in order to capture torsion. A matrix mapping the modal acceleration to the location of the sensors is constructed by a rigid body splining [27], and is denoted $\mathbf{T}_{mf}$ (with $m$ for *measurement*). The dynamics of the sensors are negligibly fast. Only the dead time introduced by the sensors is modeled. Combined with the delay of the controller, the introduced dead time is estimated to be 4 ms, yielding a total of 8 ms in the feedback loop [10]. Figure 3b depicts the location of the sensors.

## III. Gust Modeling using the Loewner Framework

Once the model of the flexible wing itself is derived, this model must be enhanced by a representation of the gust disturbance, to design the GLA controller and validate its performance. A separate section is dedicated to the gust model to be able to discuss the novel approach of the Loewner framework in detail, although the gust is only another external aerodynamic force in Eq. 1. From the DLM, frequency domain data is available. However, the RFA as presented in Section II.D is unsuited for application on the gust AIC column [33]. The reason for this unsuitability is the time delay in gust aerodynamics as described by the Sears function [22], creating a spiral pattern when plotting real over imaginary part. The Loewner framework is one option to address the frequency to time domain transformation of gust aerodynamics, as it can identify a state-space system from given frequency domain data.

### A. Gust Definition and Gust Model in the Frequency Domain

In the certification documents (EASA CS-25, [20]) a discrete gust design criterion is given. The so-called vertical *1-cos gust*, to be used to quantify gust loads, is defined as:

$$w^G(t) = \begin{cases} \frac{U_{ds}}{2 \cdot U_\infty} \cdot \left(1 - \cos\left(\frac{2\pi \cdot U_\infty \cdot t}{2 \cdot H}\right)\right) & t_s \leq t \leq t_e, \\ 0 & \text{otherwise}, \end{cases} \tag{9}$$

with $U_{ds}$ being the design gust velocity, $H$ the gust gradient (half gust length), $t_s$ the start time, and $t_e$ the end time of the gust encounter. In the certification documents the relevant gust gradients are given as 9 – 107 m. For the wind tunnel test the gust gradients need to be scaled according to the geometric scale of the model, yielding 0.45 – 5.35 m. The amplitude of the gust $U_{ds}$ depends on characteristics of the respective aircraft, see Ref. [20]. Figure 4 presents the range of gusts that will be relevant for the oLAF wind tunnel experiment, with the according gust amplitudes.

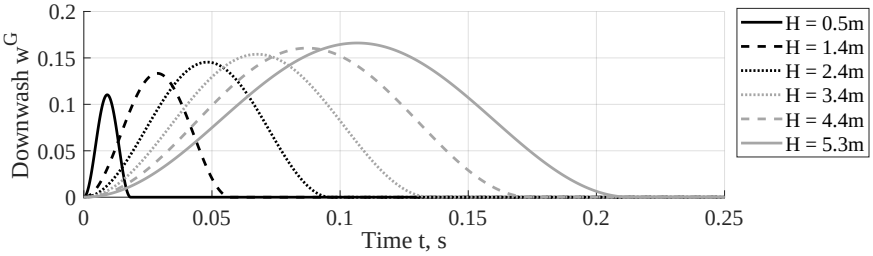


**Fig. 4 Gust profiles used in the oLAF experiment**

Now that the gust profile is defined by Eq. 9, the interaction of the gust with the aircraft needs to be modeled. The aim is to compute a gust load vector $\mathbf{P}_g^G$ that acts as an external force on the right hand side of the flexible EOM, Eq. 1. A gust-AIC column from the downwash at each panel $\mathbf{w}_j^G$ to the structural loads $\mathbf{P}_g^G$ is derived in the frequency domain using the DLM, where $k_G$ is the reduced gust frequency [14]:

$$\begin{aligned} &\mathbf{P}_g^G(k_G) = q_\infty \cdot \mathbf{Q}_g^G(k_G) = q_\infty \cdot \mathbf{Q}_{gj}(k_G) \cdot \mathbf{w}_j^G(k_G) = q_\infty \cdot \mathbf{T}_{kg}^T \cdot \mathbf{S}_{kj} \cdot \mathbf{Q}_{jj}(k_G) \cdot \mathbf{w}_j^G(k_G), \\ &\mathbf{w}_j^G(\omega_G) = \nu_G(\omega_G) \cdot e^{\left(-i\omega_G \cdot \frac{\mathbf{x}_j}{U_\infty}\right)} \cdot \mathbf{n}_j. \end{aligned} \tag{10}$$

In this equation $\mathbf{x}_j$ is the location of the three-charter-chord points ($j$-set) of each aerodynamic panel, $\mathbf{n}_j$ are the panel normal vectors, and $\nu_G(\omega_G)$ is the gust spectrum. This spectrum shall be unit, meaning that there is a sinusoidal motion with unit amplitude present at any gust encounter frequency, and an arbitrary gust signal may be composed in the time domain by superposition. The exponential term in Eq. 10 is nothing else than a time delay or phase shift $e^{-st}$ with the time variable replaced using the geometric location $\mathbf{x}_j$.

### B. Loewner Framework for State-Space Representation of the Gust

For gust aerodynamics RFAs yield inadequate results, as they are not well-suited for time delays [33], hence the Roger's RFA is unsuited to transfer the gust loads to the time domain. The Loewner framework turned out to be a well-working alternative. The resulting gust model is of low order, which is beneficial for controller design with $\mu$-synthesis, as the order of the controller is equal to the one of the plant. The theory of the framework is derived in Ref. [17, 34, 35]. It has already been applied for example in Ref. [9, 33].

The Loewner algorithm is fed with frequency domain data from Eq. 10, provided as a pair of frequencies and matrices $\{s_i, \mathbf{Q}^G_{g,i}(s_i)\}, i = 1 \ldots n$. To produce a good-matching system approximation with the Loewner framework the number of data pairs shall be high, $n \approx 1000$ has shown to be sufficient. The frequency domain data is supplied to the Loewner algorithm, which approximates the system by a descriptor state-space system. The tangential directions are chosen to be Gaussian randomly distributed numbers, as Ref. [36] proposed, which yielded good results. To ensure reproducibility when applying the Loewner framework the random numbers are generated using a certain seed. The order of the system is controlled by the number of singular values taken into account. From inspection an order of 25 proved sufficient. The resulting state-space system in descriptor form can be re-written in the standard state-space form by inverting the **E**-matrix (which must be non-singular and hence invertible):

$$\begin{aligned} \dot{\mathbf{x}}^G &= \mathbf{E}^{-1}_{gust} \cdot \mathbf{A}_{gust} \cdot \mathbf{x}^G + \mathbf{E}^{-1}_{gust} \cdot \mathbf{B}_{gust} \cdot w^G(t), \\ \mathbf{P}^G_g(t) &= q_\infty \cdot \mathbf{C}_{gust} \cdot \mathbf{x}^G. \end{aligned} \tag{11}$$

Equation 11 can be supplied with the gust input $w^G(t)$ and provides the gust loads $\mathbf{P}^G_g$ that enter the flexible EOM. The matrices of the resulting system are real, which is guaranteed by a transformation in the Loewner framework [17].

### C. Stabilization of the Identified System

It might occur that the descriptor system resulting from the Loewner algorithm is not stable. This needs adjustment as otherwise the response of the state-space system to a certain input would become unbounded. In Ref. [37] Koehler develops a $H_2$ or $H_\infty$ optimal stabilization. Applying this technique shows that omitting the unstable poles completely yields the optimal solution with respect to the $H_2$ or $H_\infty$ norm. However, the dynamics are changed quite significantly depending on the location of the unstable poles. Another technique of Ionita [36] proposes to negate the real part of the unstable poles. This ensures the dynamics of the system are kept as far as possible, but an error is introduced due to the change of the real part. For this paper, Ionita's technique is favored. To obtain only real matrices, the transformation procedure described in Ref. [17] can be used once again.

During the stabilization the real parts of the unstable poles are negated. This changes the dynamics of the system. Especially the steady-state response might be off, where the real part is the dominating factor for aerodynamic forces. Since an exact steady-state solution is generally required, this needs to be corrected. The **D**-matrix can be used for this purpose. By adding the steady-state difference between the originally identified system from Eq. 11 and the stabilized system to the **D**-matrix, the steady-state error returns to zero. Finally, the stabilized state-space system reads:

$$\begin{aligned} \dot{\mathbf{x}}^G_{stab} &= \mathbf{E}^{-1}_{gust,stab} \cdot \mathbf{A}_{gust,stab} \cdot \mathbf{x}^G_{stab} + \mathbf{E}^{-1}_{gust,stab} \cdot \mathbf{B}_{gust,stab} \cdot w^G(t), \\ \mathbf{P}^G_g(t) &= q_\infty \cdot \mathbf{C}_{gust,stab} \cdot \mathbf{x}^G_{stab}. \end{aligned} \tag{12}$$

### D. Exemplary Results of the Loewner Gust Approximation

The Loewner framework provides very satisfactory results to identify a state-space model for gust aerodynamics and loads. This can be seen by comparing the exact nonlinear computation from Eq. 4 with Eq. 5 to the resulting loads from the Loewner identified and stabilized system from Eq. 12. This comparison is shown in Figure 5. Additionally, the results of the approximation obtained by Roger's RFA are shown.

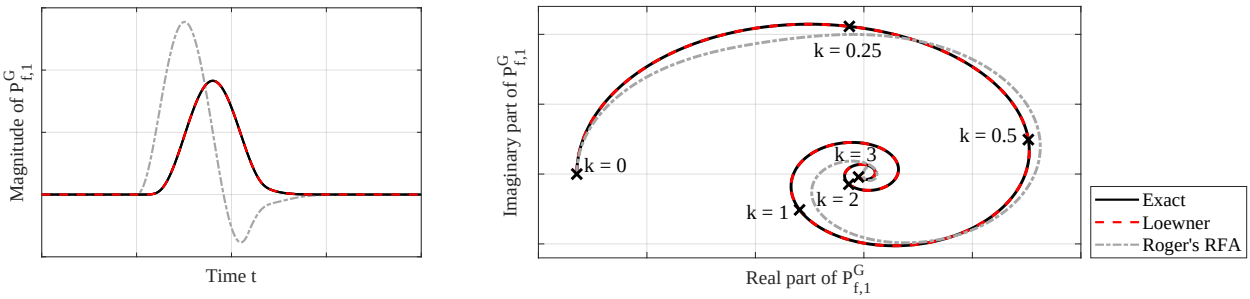


**(a) Time domain** **(b) Frequency domain**

**Fig. 5 Comparison of exact gust with Loewner approximation and Roger's RFA**

Figure 5a shows the time response of the first entry $P_{f,1}$ of the generalized forces, resulting by pre-multiplying the structural force with the eigenvector matrix $\mathbf{\Phi}_{gf}^T$. There is virtually no difference visible between exact and approximated loads, confirming the excellent approximation achieved with the Loewner framework and only 25 states. The RFA yields unsuitable results, as anticipated.

The comparison can also be conducted in the frequency domain, which is shown in Fig. 5b, again for the first entry of the generalized forces. Plotting real over imaginary part reveals the spiraling behavior of the underlying Sears function [22], and again the Loewner approximation yields an excellent approximation. The same observation is made for the other entries of the generalized forces, which are omitted here for practical reasons.

Compared to other methods like an approach using Padé elements to approximate the time delay of the gust aerodynamics [38], the Loewner framework produces a more exact approximation at a lower number of states. The stabilization ensures a useful resulting state-space system. The Loewner framework proved to be a beneficial addition to aeroservoelastic modeling.

## IV. Nonlinear Model, Linear Model, and Order Reduction

The above derived ingredients of the model are finally combined to yield the overall aeroservoelastic model. Two types of models of the oLAF experimental wing are being established (the differences are described below):

1) a nonlinear model for time domain simulations and controller validation,
2) a linear state-space model for controller synthesis.

### A. Nonlinear Model for Validation

The nonlinear simulation model is implemented within MATLAB-Simulink. This model creates a virtual representation of the wind tunnel experiment, freestream velocity and gust conditions are adjustable. The aeroservoelastic model developed in Section II is the core of the simulation, the gust disturbance modeled by the Loewner Framework (Section III) is added. The forces and moments at the wing root are calculated using the force summation method, as detailed at the beginning of Section II.

Actuator limits in deflection, rate, and acceleration are applied. The dead time in the feedback loop due to sensors, actuators, and the controller, is considered. Noise may be added to the sensor measurements. Additionally, a rigid body motion in pitch can be enforced. Gravity acting on the flexible wing is taken into account. In this model the controller is validated after the synthesis (Section VI), to assess the performance in realistic conditions. The nonlinearities in form of limits, dead time, noise and enforced motion are adjustable, to study the effect on controller performance.

### B. Linear Model For Controller Synthesis

The linear state-space model for controller design is derived from the nonlinear model. The linearization is performed around a typical cruise pitch angle of 3° at a freestream velocity of 50 m/s. Nonlinearities are obviously not present, meaning actuator limits, dead time, rigid body motion and gravity is not taken into account in controller synthesis. The inputs of the state-space model are the gust disturbance as well as the control surface commands, the outputs are the cut-loads at the wing root as well as the acceleration measurements. The cut-loads are calculated using the force summation method, see Eq. 2.

### C. Model Order Reduction of the Linear Model

For controller synthesis the linear state-space model should be reduced to obtain a model that achieves the necessary accuracy with as few states as possible. The synthesis algorithms generally work better for lower order plants. Furthermore, for the synthesis method used in this paper ($H_\infty$-control) the size of the controller depends on the size of the plant. Thus it is useful to minimize the number of states by a model order reduction (MOR) technique. Balanced truncation [39, 40] is chosen as MOR technique. The linear model is composed such that the input-output relations are as small as possible, only the inputs and outputs necessary for controller design are kept. This improves the MOR. The system is reduced from 235 to 75 states. A lower order model is possible but would jeopardizes the accuracy of the model. If the hardware in the wind tunnel experiment cannot handle the order of the designed controller, the reduced order model can be re-adjusted and the controller re-synthesized.

## V. Robust Control Synthesis

The aeroservoelastic plant is now used for model-based controller design. The method chosen is $\mu$-synthesis, also called $D$-$K$-iteration, a multiple input multiple output (MIMO) robust control technique. This method allows to include model uncertainties within the synthesis, and thereby ensure robustness requirements necessary in controller development. An optimal solution is found for the combination of multiple sensors and control surfaces available to the controller. In $\mu$-synthesis, an iteration between optimal controller design using $H_\infty$-synthesis ($K$-step) and $\mu$-analysis with scaling of the plant ($D$-step) is conducted. Thus one obtains a controller with desired performance characteristics while being robust to plant uncertainties, i.e. achieving *robust performance*. As the name of the synthesis method indicates the structured singular value $\mu$ for robust performance is minimized. [41]

In robust control, the control framework is formulated in a standard form [13, 41], in which a generalized plant **P** with certain exogenous inputs **w** and exogenous outputs **z** is interconnected with a controller **K** by feedback variables **v** and control variables **u**. Uncertainties are captured within a **Δ**-matrix, which is added as another loop to the generalized plant, using the uncertainty inputs $\mathbf{u}_\Delta$ and outputs $\mathbf{y}_\Delta$ [13]. This structure and two adaptations - in which the closed loop system is abbreviated as **N**, and the performance loop closed over $\mathbf{\Delta}_p$ - are shown in Fig. 6.

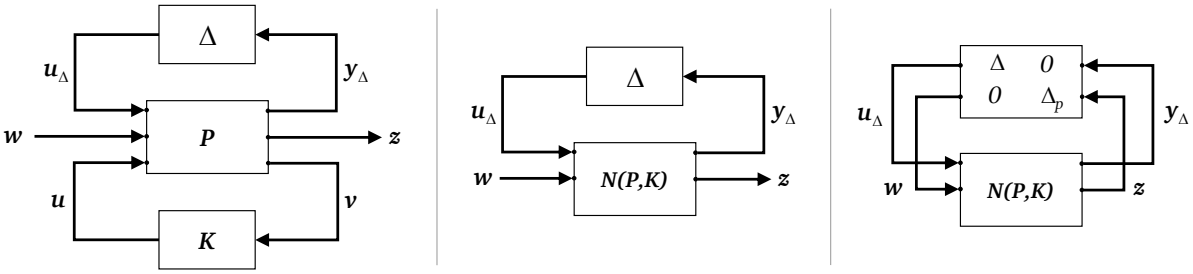


**Fig. 6 General robust control framework in three formulations, adapted from [13]**

A robust control technique like $\mu$-synthesis is well suited for GLA, it allows to shape the closed loop system to provide stability and robustness margins. The model of the flexible aircraft contains errors due to assumptions, unmodeled effects, neglected dynamics, changing operating conditions and disturbances occurring in flight. Ensuring robustness is consequently a key requirement for the GLA functions.

The controller synthesis will be performed using the reduced order model, to obtain a controller with a low number of states. For validation, the controller will be integrated into the nonlinear simulation using the full order model.

### A. Control targets

The generalized plant for gust load alleviation with the respective exogenous inputs and outputs as well as uncertainties needs to be composed such that the desired control targets can be reached. The GLA control should:

1) reduce integral loads at the wing root: wing-root bending moment (WRBM) and wing-root torsion moment (WRTM), the reduction of the WRBM is prioritized,
2) ensure stability of the closed loop system,
3) ensure robustness against uncertainties in the modeling, changing operating conditions and output disturbances due to sensor measurements,
4) work for the entire range of gust gradients defined as well as other atmospheric disturbances,
5) minimize control activity and limit bandwidth of the controller.

Obviously, these control targets are not congruent and pose a trade-off problem. The first target is performance oriented. The integral loads at the wing root shall be reduced, as these loads are typically the driver for the structural weight. A criterion on local loads is not added to the synthesis setup, but checked a posteriori. Stability of the closed loop system is mandatory, and additionally the controller itself shall be stable. In $H_\infty$-synthesis this is not automatically guaranteed, but it is necessary so that the controller works in the full order system. Here, the definition of uncertainties and a design for robustness within $\mu$-synthesis helps compared to pure $H_\infty$-synthesis.

The fourth target demands that the controller works for the range of gust gradients from 0.5 to 5.5 m - scaled to match the wind tunnel model size. Although tailored to the vertical *1-cos-gust* defined in the certification specifications, the aim is that the controller copes with any form of atmospheric disturbance, also continuous turbulence.

The fifth target ensures the practical applicability of the designed controller, avoiding the interaction with primary flight control and the excitation of higher order flexible modes.

**B. Generalized Plant**

The generalized plant is set up in a way to fulfill the control targets specified previously. At the core of the generalized plant is the (reduced order) aeroelastic model **G** developed in Sections II through IV. Uncertainties at the input and output of the plant are taken into account, representing actuator and sensor uncertainties. The exogenous input **w** of the generalized plant will be the gust, i.e. $\mathbf{w} = w^G$. The exogenous outputs **z** will be:

1) $\mathbf{z}_1$: performance output, from the gust to the wing-root loads $\mathbf{P}_{\text{perf}} = [P_{\text{WRBM}}, P_{\text{WRTM}}]^T$,
2) $\mathbf{z}_2$: control output, minimization of control energy.

The performance output uses the integral loads, it will govern the controller design in a central frequency range, in which the controller shall reduce the loads due to a gust disturbance. The control output ensures that the controller does not excessively command control surface deflection. The included uncertainties ensure robustness of the controller. Figure 7 presents the composition of the generalized plant, with **H** indicating selection matrices, **w** denoting weighting filters, and **Δ** denoting uncertainties.

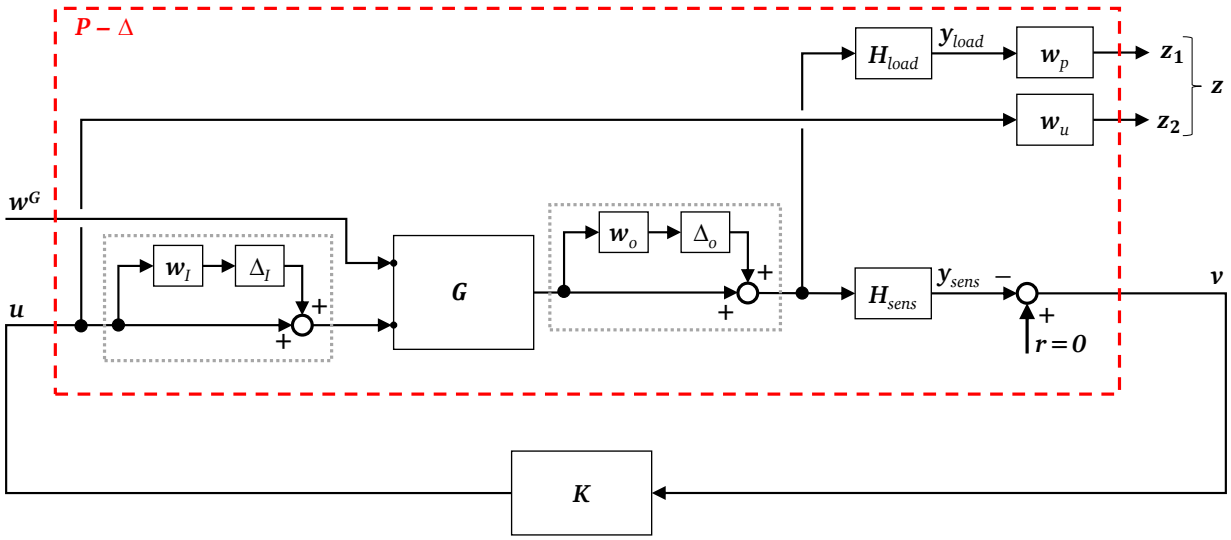


**Fig. 7 Generalized plant for gust load alleviation control**

The generalized plant with uncertainties as displayed in Fig. 7 can be formulated as the classic Δ-$P$-$K$-structure presented in Fig. 6. The uncertainties at the plant's input and output are defined as structured multiplicative uncertainties [13], separate for each channel. While a lumped (unstructured) uncertainty would reduce computation effort during the $\mu$-synthesis, it would also introduce nonphysical couplings between the individual actuators and sensors, leading to a conservative robustness requirement [13]. Complex uncertainties are employed, facilitating the solution of the optimization problem as only $D$-scaling, no $D$- and $G$-scaling is required [42, 43]. A posteriori, a $\mu$-analysis with real uncertainties is conducted. The resulting **Δ**-matrix is of size 15 and contains complex uncertainties along its diagonal, with the $H_\infty$-norm of the matrix being no larger than one.

The main task now is to select the weighting filters to fulfill the control targets. The filter adaption is an iterative process. After a conducted synthesis the result is evaluated and - if needed - the filters are adapted. For example, if more robustness is needed, the uncertainty weights can be increased and the performance weight decreased. This process is repeated until the result is satisfactory. Described here is the final outcome of the iterative selection process. The weighting filters are presented in figure 8.

Starting with the uncertainty weights $\mathbf{w}_I$ at the input (actuators) and $\mathbf{w}_o$ at the output (sensors). The actuator uncertainty can be modeled physically [44], based on expectations of the actuator behavior. Here it is chosen to incorporate 5% uncertainty in actuator deflection in the lower frequency regime and 10% at higher frequencies, the increase in uncertainty at 45 rad/s - which is half the actuator bandwidth, based on Ref. [44]. The sensor dynamics feature are modeled with a similar uncertainty weight, however the values are chosen to be 2.5% at low and 5% at high frequencies, the increase located at 90 rad/s.

The performance weight $\mathbf{w}_p$ is chosen to minimize the loads resulting from a gust in the central frequency domain, from $2 \cdot 10^1$ to $10^2$ rad/s. The WRBM shall be reduced more than the WRTM. A roll-off to low and high frequencies is

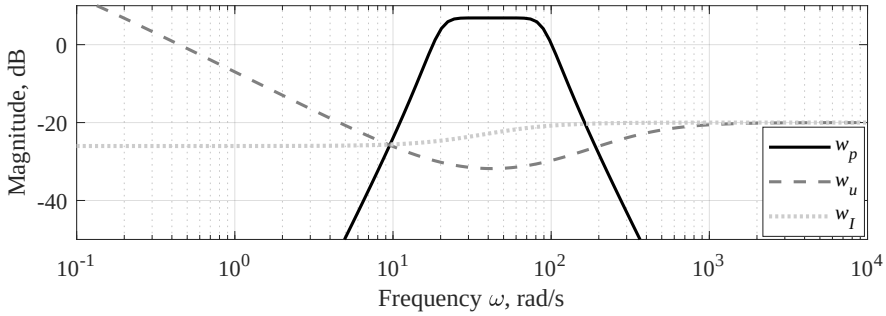


**Fig. 8 Weighting filters used in the generalized plant**

introduced, to avoid the controller trying to minimize the loads in the steady-state region, and in the high frequency region where higher order modes have only little impact on the loads.

The control activity weight $\mathbf{w}_u$ is chosen to be somewhat inverse to the performance weight. Low frequencies are penalized to avoid the controller being active in the low frequency domain where it could command steady deflections of the control surfaces. The actuators feature a roll-off at 90 rad/s, loosing their effectiveness, thus high frequencies are penalized as well.

### C. Performance and Robustness Using the Structured Singular Value $\mu$

The aim of robust controller design using $\mu$-synthesis is to achieve robust performance. The structured singular value (SSV) is applied in $\mu$-analysis [45] to assess stability and performance of the closed loop system. Linear fractional transform (LFT) are a useful tool for these analyses.

Starting with the left representation of the system in Fig. 6, a lower LFT is used to obtain the closed loop uncertain system $\mathbf{N} = \mathbf{F}_l(\mathbf{P}, \mathbf{K})$, in which the exogenous inputs $\mathbf{w}$ and outputs $\mathbf{z}$ are free, see central depiction in Fig. 6. This configuration allows to test for robust stability by performing a $\mu$-analysis, i.e. $\mu_\Delta(\mathbf{N}_{11})$, with $\mathbf{N}_{11}$ being the transfer function from $\mathbf{u}_\Delta$ to $\mathbf{y}_\Delta$. Also, nominal performance can be assessed by the singular values of $\mathbf{N}_{22}$, connecting $\mathbf{w}$ and $\mathbf{z}$. The requirements are fulfilled if $\mu < 1$. Nominal stability is always guaranteed by the synthesis. [13]

For robust performance analysis an upper LFT can then be applied on the closed loop system, closing the free exogenous inputs and outputs with a performance uncertainty $\Delta_P$, as seen on the right in Fig. 6. If one defines the appended uncertainty as $\bar{\mathbf{\Delta}} = \text{diag}(\mathbf{\Delta}, \mathbf{\Delta}_P)$, it holds: $\mathbf{F}_u(\bar{\mathbf{\Delta}}, \mathbf{N})$. Robust performance is achieved once $\mu_{\bar{\mathbf{\Delta}}}(\mathbf{N}) < 1$ [13]. It shall be noted that for a meaningful nominal and robust performance analysis an adequate scaling of the plant is required. The performance output has to be scaled such that a performance level of one means the requirements are fulfilled. If this level is achieved with uncertainties, the performance requirement is robustly achieved.

### D. Controller Synthesis

The $\mu$-synthesis ($D$-$K$-iteration) algorithm as presented in Ref. [13, 41] allows to find an optimal controller that minimizes the SSV $\mu$ for robust performance, i.e. $\mu_{\bar{\mathbf{\Delta}}}(\mathbf{N}(\mathbf{P}, \mathbf{K}))$. If this value is smaller than one, this means that desired (specified) performance targets of the closed loop system are met, even with the highest possible uncertainty in the system. Since the SSV cannot be computed exactly, it is approximated by upper (and lower) bounds [46] in the form of $\mu(\mathbf{N}(\mathbf{K})) < \min \bar{\sigma}(\mathbf{D}\mathbf{N}(\mathbf{K})\mathbf{D}^{-1})$. The synthesis problem is hence to find a stabilizing controller $\mathbf{K}$ that minimizes the norm $\|\mathbf{D}\mathbf{N}(\mathbf{K})\mathbf{D}^{-1}\|_\infty$ of the closed loop system [41]. A two step process as applied, iterating between controller design ($K$-step) and $\mu$-analysis with $D$-scaling of the plant $\mathbf{N}$ ($D$-step) [41].

To obtain the controller, $H_\infty$-synthesis [47] is used. To take care of the uncertainties, the $H_\infty$-norm supplied is not only the one taken from exogenous inputs $\mathbf{w}$ to outputs $\mathbf{z}$, but instead between $[\mathbf{u}_\Delta, \mathbf{w}]^T$ and $[\mathbf{y}_\Delta, \mathbf{z}]^T$ of the scaled plant $\mathbf{D}\mathbf{N}\mathbf{D}^{-1}$. The controller is thereby forced to also include the effect of uncertainties on the control commands. The controller avoids commands that lead to a high $H_\infty$-norm, also when caused by the uncertainty channels. During the $K$-step the $D$-scales on the plant are held constant.

After each control synthesis, the frequency-dependent $D$-scales of the plant are adapted by the outcome of a $\mu$-analysis for robust performance ($D$-step), i.e. for the plant $\mathbf{D}\mathbf{N}\mathbf{D}^{-1}$ closed with $\bar{\mathbf{\Delta}} = \text{diag}(\mathbf{\Delta}, \mathbf{\Delta}_P)$. This is the essence of $\mu$-synthesis. By scaling the plant, the way the uncertainties interact with the plant is adapted and hence the controller is

informed how to minimize the effect of uncertainties. To keep the order of the resulting system low [47], the $D$-matrices are approximated by low order transfer functions [13]. It shall be noted that the synthesis is not jointly convex, but only the individual steps ($D$- and $K$-step) [41]. The process of $D$-$K$-iteration is repeated until a satisfactory result is obtained. This could be a SSV $\mu < 1$ or a no longer decreasing $H_\infty$-norm, indicated by the value $\gamma_{min}$.

Applied to the GLA problem at hand, the $\mu$-synthesis yields the results depicted in Fig. 9, after six $D$-$K$ iterations. Shown is the frequency response of the maximum singular value $\bar{\sigma}$ of the closed loop **N** and open loop **P**, i.e. from exogenous input **w** to output **z**. Figure 9a includes no weighting functions $\mathbf{w}_u$ and $\mathbf{w}_p$, while these are taken into account in Fig. 9b. The minimum achievable $H_\infty$-norm is indicated by the level $\gamma_{min}$.

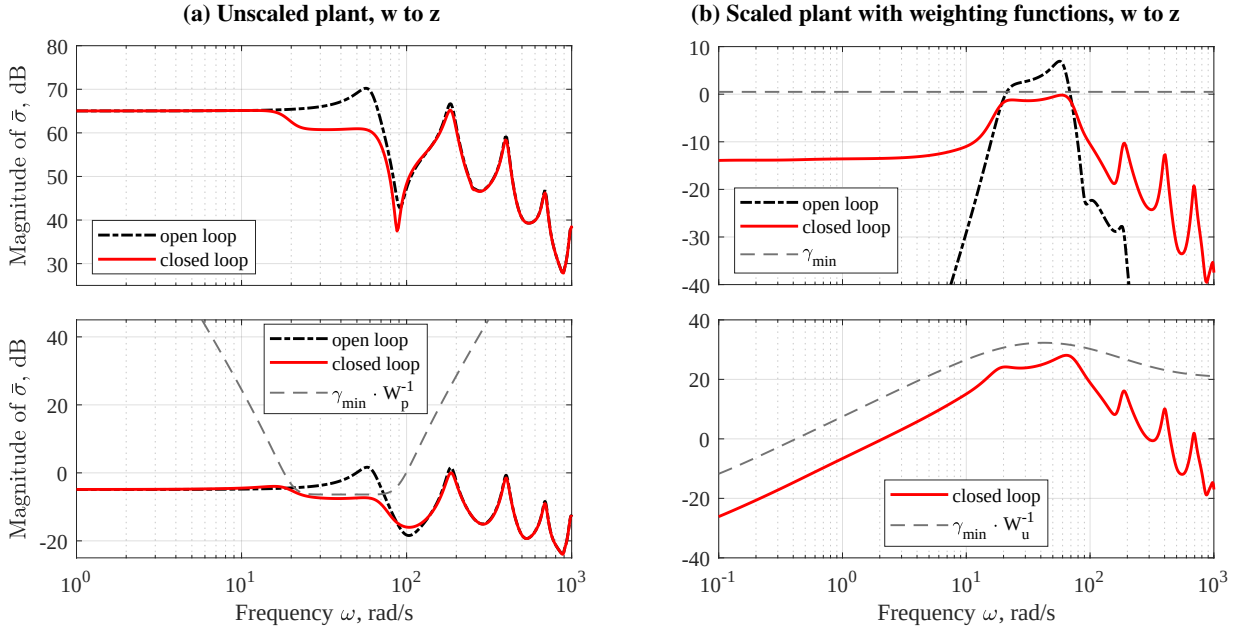


**Fig. 9 Max. singular value $\bar{\sigma}$ of open and closed loop from w to z**

The norm is successfully reduced in the frequency range from 20 to 70 rad/s. The first eigenmode at about 55 rad/s is reduced in magnitude. Figure 9b furthermore shows the trade-off in frequency regimes: to reduce the norm in the relevant frequency range it is necessary to increase it in other frequency regimes. The roll-off to low and high frequencies in the performance weight is permitting this increase. The analysis of Fig. 9b does not reveal robustness properties, for which the norm with uncertainties would need to be examined, see Section VI.C.

To show that the controller shapes the closed loop system not only bound by the performance requirements but also following control activity requirements, Fig. 9c and 9d present the open and closed loop transfer function split into its channels $\mathbf{z}_1$ for performance and $\mathbf{z}_2$ for control activity. Figure 9c shows the shaping of the closed loop by the performance weight $\mathbf{w}_p$, and Fig. 9d the shaping due to the control activity weight $\mathbf{w}_u$. The controller design includes both weights appropriately.

## VI. Evaluation of the Designed Controller

The designed controller is evaluated in the nonlinear simulation using the full order model. A time delay of 8 ms is present in the feedback loop, originating from the controller, the sensors and the actuators. The actuators are limited in deflection at 10°, in rate at 1129°/s and in acceleration at 75000°/s$^2$ [31]. These constraints are taken into consideration when designing the controller, for example robustness is induced to cope with the time delay. To evaluate the performance of the controller, time domain simulations are conducted. The simulated wing is in cruise condition, at which a steady-state load already exists due to a 3° angle of attack. The freestream velocity is set to 50 m/s.

### A. Performance Evaluation

Figure 10 presents the (integral) bending and torsion moment at the wing root. A gust with a gradient H of 3 m is perturbing the wing. Other gust lengths are tested further below. The figure shows a successful reduction of the maximum load, when comparing the system with and without gust load alleviation control. The peak in WRBM can be reduced by 20% when referring to the overall load level. When taking the steady-state load level of 166 Nm as a starting point, the reduction is 32%. The WRBM is lower in the controlled system for the entire time, also during the oscillations following the primary deflection. The WRTM is also reduced, by 12% (25%) for the peak in the torsion moment. The structural behavior of the swept wing is favorable for the torsion moment with GLA, as the negative moment present in the open loop alleviates the moment induced by the control surface deflection upwards.

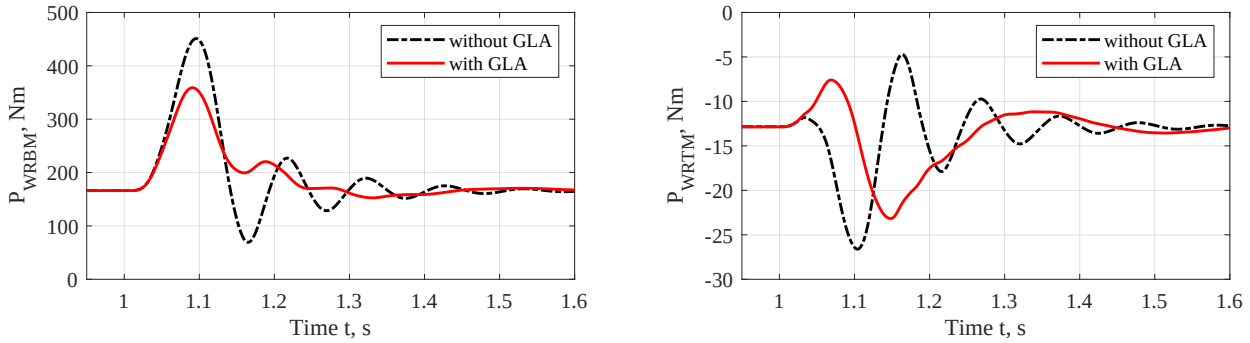


**(a) Wing-root bending moment** **(b) Wing-root torsion moment**

**Fig. 10 Time response of WRBM and WRTM for a gust with H = 3 m**

Besides the integral loads shown in Fig. 10, it is also checked that the commanded control surface deflections do not induce local loads that are higher than in the case without GLA. This is not the case. The wing is quite rigid as it is a wind tunnel model. For a full scale wing that is more flexible, local loads need to be thoroughly examined.

The load alleviation is achieved by deflecting the control surfaces, as shown in Fig. 11. An upwards deflection of the control surfaces reduces lift by adding negative camber, thereby reducing the bending moment at the wing root. The commanded deflection of the five available control surfaces is quite similar.

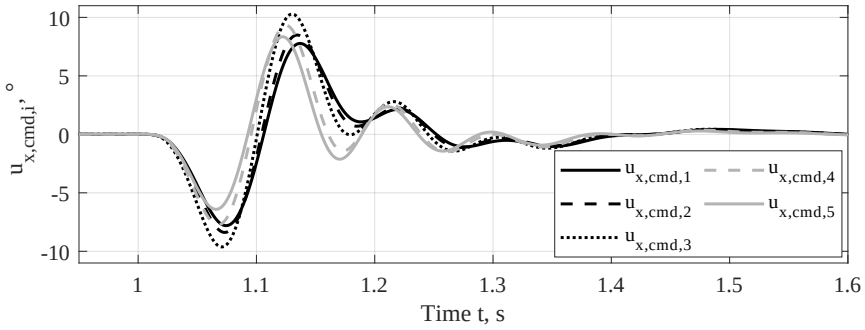


**Fig. 11 Commanded control surface deflections for a gust disturbance with H = 3 m**

The maximum deflection of the control surfaces does not exceed 10°, which was set as the maximum. Saturation does not pose a problem in deflection, rate, and acceleration. In a setup with less control surfaces available for GLA, for example only the outer ailerons, this might change. It can be seen that control surface three (located mid wing) is deflected the most, followed by control surfaces two and four. The individual deflection depends on the position, i.e. lever arm, and size of the surfaces. It shall be noted that by an individually adapted weighting function $\mathbf{w}_u$ the usage of the different control surfaces can be altered if desired.

The controller fulfills the target of working for a range of gust gradients. The relevant gust gradients were determined to lie between 0.45 and 5.35 m. Table 1 presents the reduction in peak WRBM for four gust gradients within the range of interest. The controlled system shows a similar reduction in maximum WRBM of about 20% for all gust lengths

(about 30% when the steady-state load is taken as the reference), compared to the uncontrolled system. A gust gradient smaller than 1 m induces a load pattern that differs from the *1-cos* for the first peak. The controller still works, but a test with such small gust gradients does not seem useful for GLA evaluation.

**Table 1 Influence of the gust length on bending load reduction**

| Gust gradient H, m | max. WRBM, Nm without GLA | max. WRBM, Nm with GLA | absolute change $\Delta$, Nm | relative change $\delta$, 1 | max. control deflection, ° |
|---|---|---|---|---|---|
| 2.0 | 381 | 309 | -72 | -19% (-34%) | 8.7 |
| 3.0 | 451 | 359 | -92 | -20% (-32%) | 8.9 |
| 4.0 | 480 | 384 | -96 | -20% (-31%) | 8.1 |
| 5.0 | 487 | 384 | -87 | -18% (-27%) | 7.6 |

The fact that the controller works well for a range of gust gradients can also be observed when analyzing the frequency response in WRBM due to a gust input. This frequency response is computed using the linear state-space model of full order, and is presented in Fig. 12. In the relevant range from 20 to 70 rad/s the GLA control achieves a significant reduction in magnitude. The magnitude of the frequency response around the frequency of the first bending mode at about 55 rad/s is particularly decreased. This underlines the importance of damping the first bending mode for gust load alleviation. The higher order modes contribute significantly less to the integral load.

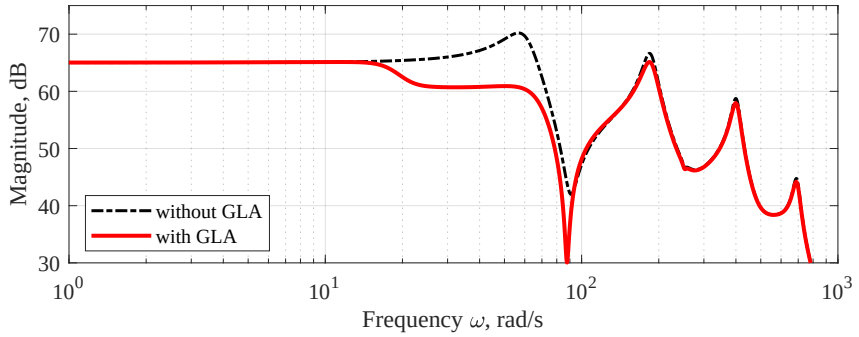


**Fig. 12 Magnitude frequency response from a gust input to the WRBM**

Besides the frequency response of the WRBM, especially the frequency response from a gust to the control commands allows insight into the workings of the controller. This transfer function is presented in Fig. 13. This is the controller transfer function superimposed with the transfer function from gust to sensors. It becomes clear that the controller is most active around the peak at 55 rad/s, the first bending mode. Magnitude drops towards low and high frequencies, obeying the increasing control activity weight as well as decreasing performance weight.

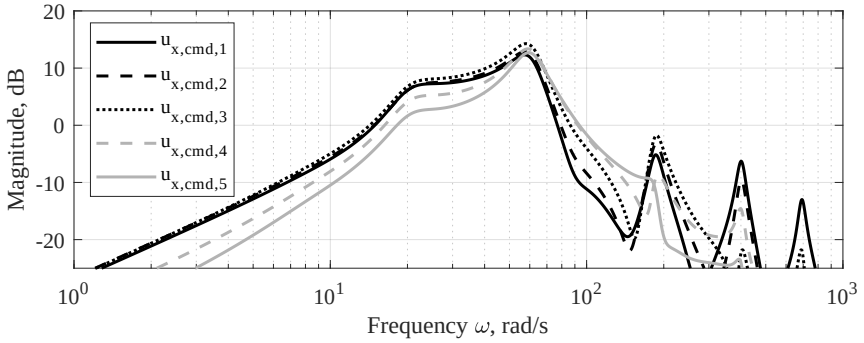


**Fig. 13 Frequency response from gust input to control commands**

The roll-off below 20 rad/s is important to avoid slow moving control surfaces, i.e. slow poles. This was an undesired behavior observed in previous iterations of the controller design. As uncertainties increase towards higher frequencies

(see $w_I$ in Fig. 8), the roll-off in the controller transfer function towards higher frequencies ensures robustness. By inspection one can see that the controller transfer function is shaped similarly to the performance weight, and inversely to the control activity weight, something that has already been discussed in Section V.D, with Fig. 9c and 9d.

### B. Effect of the Time Delay and Noise

The controller shall also work under non-ideal conditions, like included time delay and noise. A time delay of 8 ms is present in the feedback loop, and the controller works well for this delay, as presented in the previous section. The robustness incorporated in the synthesis ensures that a certain time delay does not cause the controller to perform poorly. Due to input and output uncertainties, a certain phase margin is guaranteed. However, when the time delay is too large, the closed loop system can be rendered unstable. At 8 ms, the performance is almost identical to the one without any time delay. However, at $T_{del} > 15$ ms, the performance begins to degrade, and the damping of the modes is reduced. This is shown in Fig. 14a. Hence, the delay in the system shall be kept as small as possible. This would allow to reduce robustness requirements and increase performance.

When moderate noise is introduced into the system - in the sensor measurements - the controller still performs well. This is presented in Fig. 14b, where the WRBM time response for a system with noise is shown. The variance of the noise is $\sigma = 0.1$, typical for an acceleration sensor. The load reduction potential is not visibly reduced by this noise. Thus, it can be expected that the controller will work also in a real hardware setup.

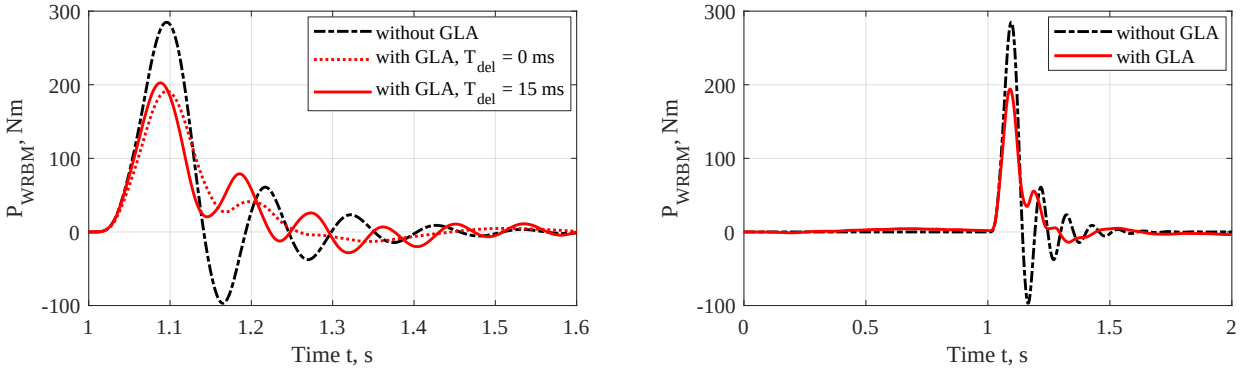


**(a) Time delay** **(b) Sensor noise**

**Fig. 14 Effect of time delay and noise on the GLA functionality**

### C. Robustness Evaluation using Disk Margins

The robustness can be evaluated using $\mu$-analysis. The theoretic background is given in Section V.C, as well as in Ref. [13, 45]. Figure 15 shows the evaluation of robust stability, nominal performance and robust performance. Nominal stability is mandated as an outcome of the $\mu$-/$H_\infty$-synthesis [47]. Robust stability is analyzed for the specified uncertainties at the actuator and the senors. Robust stability is investigated using a real $\mu$-synthesis, replacing the complex uncertainties (introduced for easier computation) with real uncertainties, which are physically interpretable.

Robust stability reaches a maximum of $\mu = 0.1$ at about 74 rad/s, located slightly higher than the highest controller activity at the 55 rad/s peak. As the specified uncertainties are not larger than 10% for the actuator and 5% for the senors, the maximum value of $\mu$ is quite small. The value of $\mu < 0.1$ means that uncertainties even ten times as large as the ones specified will not lead to an unstable system [13]. This can be checked by evaluating the entries of the worst case $\Delta$-matrix, i.e. the matrix that would render the system unstable. The entries are of similar magnitude and in the order of ten, the inverse of the maximum SSV [45]. Stability is ensured with a large margin, presuming the specified uncertainties are sufficiently large, which needs to be investigated when data from actuator tests is available.

Nominal performance is achieved if the maximum singular value is below one. The permanence target has to be defined a priori, and the performance weight $\mathbf{w}_p$ chosen such that the $H_\infty$-norm drops below one if the target is fulfilled. Here, the performance target is chosen to be a reduction of 20% in peak WRBM in the frequency domain, i.e. at 55 rad/s, which is fulfilled, see Fig. 9b. Robust performance is also fulfilled, since the curve lies below one, i.e. $\mu_{\tilde{\mathbf{\Delta}}}(\mathbf{N}) < 1$ (see Section V.C). This means that the performance target is not only obtained for the nominal plant, but also for the uncertain plant with all possible variations. This result is very satisfactory.

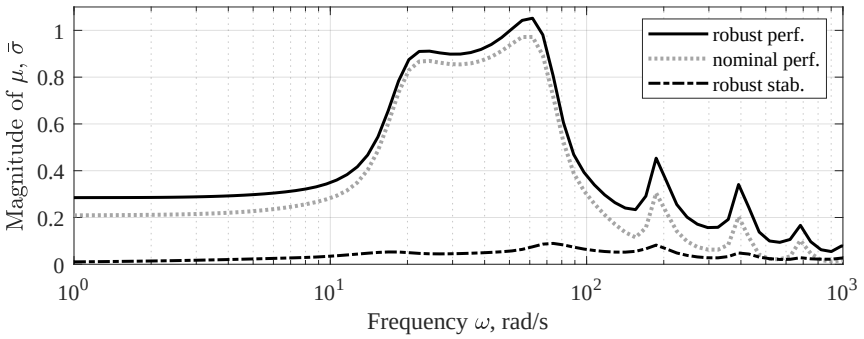


**Fig. 15 $\mu$-analysis for robust performance, nominal performance, and robust stability**

To additionally evaluate the robustness of the system, disk-based stability margins [48] are used. Both multiloop as well as loop-at-a-time margins are analyzed. Table 2 summarizes the disk-based gain and phase margins computed for input and output open loop, in absolute units for gain and in degrees for phase. The displayed loop-at-a-time margins are for the worst case among all the loops.

**Table 2 Disk-based stability margins of the open loop transfer function**

| Type | Cut point | Disk-based gain margin | Disk-based phase margin | Frequency | Worst loop |
|---|---|---|---|---|---|
| multiloop | input | 0.20 \| 5.00 | −67.5° \| 67.5° | 87 $rad/s$ | - |
| multiloop | output | 0.54 \| 1.85 | −33.1° \| 33.1° | 184 $rad/s$ | - |
| loop-at-a-time | input | 0.05 \| 20.0 | −84.5° \| 84.5° | 101 $rad/s$ | $u_{x,cmd,5}$ |
| loop-at-a-time | output | 0.39 \| 2.59 | −47.7° \| 47.7° | 187 $rad/s$ | $\ddot{u}_{m,1}$ |

It is noticed that the multiloop margins are always lower than the loop-at-a-time margins, they are more conservative. The worst case loop-at-a-time margin occurs for the fifth actuator regarding the inputs and the first acceleration sensor regarding the outputs. The output margins are more constraining than the input margins. Despite the output multiloop phase margin being rather small, examining the loop-at-a-time margin reveals that most likely enough phase delay is digestible before the system becomes unstable. The robustness analysis shows that the controller has sufficient margins and can safely be deployed in the oLAF wind tunnel experiment.

## VII. Conclusion and Outlook

A gust load alleviation controller for a flexible wing to be used in a wind tunnel experiment is designed. $\mu$-synthesis as a robust control method is employed. The modeling process is described, a novel feature is the application of the Loewner framework for modeling gust loads. The Loewner framework yields very satisfactory results, it is well-suited to identify a state-space system from frequency domain gust aerodynamics. It is a promising technique to be applied not only to the gust model, but for the entire frequency to time domain transformation of aerodynamic data, possibly replacing the RFA methods.

The controller is developed using $\mu$-synthesis, with pre-defined uncertainties in actuators and sensors. The resulting controller is capable to reduce the wing-root bending moment by up to 30% compared to the load level in steady-state flight. The load reduction is achieved by deflecting five trailing edge control surfaces not more than 10°. Robustness of the controller is analyzed by $\mu$-analysis and disk-based stability margins, revealing sufficiently large margins in gain and phase, such that the controller is safe to be tested in the wind tunnel environment.

The great advantage of robust control strategies is the incorporation of robustness requirements in the synthesis process, compared to other methods where it can only be evaluated afterwards. $H_\infty$-control allows to shape the frequency response of the controller as desired, which is especially useful for flight control, with the different frequency domains that need to be avoided due to conflict with other flight control functions.

A downside of this methodology is that for MIMO systems everything is fused into a single norm, making the synthesis very sensitive to small changes in the weights. It might occur that a change in weights has only little effect on

the $H_\infty$-norm, but a quite large impact on the outcome of the synthesis. Thus, the weights need to be selected carefully. Additionally, the issue of slow moving control surfaces was quite persistent, and a sharp increase in control activity weight towards low frequencies - imitating integrative behavior - was necessary to avoid it. Time domain based methods would presumably pose less challenges in that regard, but hold other disadvantages.

The next steps include a discretization of the controller and test on actual hardware, before it will be introduced in the wind tunnel experiment in 2024. As soon as measurement data from the wind tunnel model is available, the aeroservoelastic model shall be validated and updated, to potentially adapt the GLA controller design. The addition of feed-forward control is beneficial to increase the load reduction potential, this is currently investigated. The insights gained within the oLAF project will help mature gust load alleviation functionalities for future transport aircraft.

## VIII. Acknowledgments

The oLAF project is a research project with contributions from many institutes of the DLR. Further information can be found under: `www.dlr.de/as/en/desktopdefault.aspx/tabid-17461/` [49]. The oLAF reference configuration is the outcome of a multidisciplinary design optimization. It is detailed in Ref. [50] and [51]. The oLAF wind tunnel model is derived from this configuration and defined in Ref. [12].

The structural model, CAD model (as shown in Fig. 1), as well as the aerodynamic discretization used within this paper is supplied by DLR-AE-LAE, the Institute of Aeroelastics, Department Loads Analysis and Aeroelastic Design of the German Aerospace Center (DLR). The point of contact is Johannes Dillinger, johannes.dillinger@dlr.de, research associate at said department.

## References

[1] Kretov, A., and Tiniakov, D., "Evaluation of the Mass and Aerodynamic Efficiency of a High Aspect Ratio Wing for Prospective Passenger Aircraft," *Aerospace*, Vol. 9, 2022. https://doi.org/10.3390/aerospace9090497.

[2] Xu, J., and Kroo, I., "Aircraft Design with Maneuver and Gust Load Alleviation," *29th AIAA Applied Aerodynamics Conference*, AIAA, Honolulu, USA, 2012. https://doi.org/10.2514/6.2011-3180.

[3] Binder, S., "Simultaneous Optimisation of Composite Wing Structures and Control Systems for Active and Passive Load Alleviation," PhD thesis, Delft University of Technology, Delft, Netherlands, 2021. https://doi.org/10.4233/uuid:fac93ccf-7e0b-4971-a797-d2617e378a1d.

[4] Regan, C. D., and Jutte, C. V., "Survey of Applications of Active Control Technology for Gust Alleviation and New Challenges for Lighter-Weight Aircraft," Technical Report, TM-2012-216008, NASA, 2012. URL https://ntrs.nasa.gov/citations/20120013450.

[5] Ramsey, H., and Lewolt, J., "Design Maneuver Loads for an Airplane with an Active Control System," *20th Structures, Structural Dynamics, and Materials Conference*, AIAA, St. Louis, USA, 1979, pp. 456–463. https://doi.org/10.2514/6.1979-738.

[6] Pusch, M., Ossmann, D., Dillinger, J., Kier, T. M., Tang, M., and Lübker, J., "Aeroelastic Modeling and Control of an Experimental Flexible Wing," *AIAA Scitech 2019 Forum*, AIAA, San Diego, USA, 2019. https://doi.org/10.2514/6.2019-0131.

[7] Poussot-Vassal, C., Demourant, F., Lepage, A., and Le Bihan, D., "Gust Load Alleviation: Identification, Control, and Wind Tunnel Testing of a 2-D Aeroelastic Airfoil," *IEEE Transactions on Control Systems Technology*, Vol. 25, No. 5, 2017, pp. 1736–1749. https://doi.org/10.1109/TCST.2016.2630505.

[8] Wang, X., van Kampen, E., Chu, Q. P., and De Breuker, R., "Flexible Aircraft Gust Load Alleviation with Incremental Nonlinear Dynamic Inversion," *Journal of Guidance, Control, and Dynamics*, Vol. 42, No. 7, 2019. https://doi.org/10.2514/1.G003980.

[9] Fournier, H. et. al., "Robust Gust Load Alleviation of Flexible Aircraft Equipped with Lidar," *Journal of Guidance, Control, and Dynamics*, Vol. 45, No. 1, 2022. https://doi.org/10.2514/1.G006084.

[10] Pusch, M., "Blending of Inputs and Outputs for Modal Control of Aeroelastic Systems," Ph.D. thesis, Hamburg University of Technology (TUHH), Hamburg, Germany, 2020. URL https://elib.dlr.de/139100/.

[11] Giesseler, H.-G., Kopf, M., Varutti, P., Faulwasser, T., and Findeisen, R., "Model Predictive Control for Gust Load Alleviation," *IFAC Proceedings Volumes*, Vol. 45, No. 17, 2012, pp. 27–32. https://doi.org/10.3182/20120823-5-NL-3013.00049, 4th IFAC Conference on Nonlinear Model Predictive Control.

[12] Dillinger, J., "oLAF Meilensteinbericht M-3.3, Konfiguration für LA-Demonstratorexperiment," , 2022. Internal Document, German Aerospace Center (DLR).

[13] Skogestad, S., and Postlethwaite, I., *Multivariable Feedback Control*, 2nd ed., John Wiley & Sons, Chichester, UK, 2005.

[14] Kier, T., and Looye, G., "Unifying Manoeuvre and Gust Loads Analysis Models," *International Forum on Aeroelasticity and Structural Dynamics (IFASD)*, Seattle, USA, 2009. URL https://elib.dlr.de/97798/.

[15] Hofstee, J., Kier, T., Cerulli, C., and Looye, G., "A Variable, Fully Flexible Dynamic Response Tool for Special Investigations (VarLoads)," *International Forum on Aeroelasticity and Structural Dynamics (IFASD)*, Amsterdam, Netherlands, 2003.

[16] Kier, T. M., and Hofstee, J., "VarLoads - eine Simulationsumgebung zur Lastenberechnung eines voll flexiblen, freifliegenden Flugzeugs," *Deutscher Luft- und Raumfahrtkongress (DLRK)*, DGLR, Dresden, Germany, 2004.

[17] Karachalios, D. S., Gosea, I. V., and Antoulas, A. C., "The Loewner Framework for System Identification and Reduction," *Model Order Reduction*, De Gruyter, 2021, Chap. 6, pp. 181–228. https://doi.org/10.1515/9783110498967-006.

[18] Reschke, C., "Integrated Flight Loads Modelling and Analysis for Flexible Transport Aircraft," Ph.D. thesis, University of Stuttgart, Stuttgart, Germany, 2006. https://doi.org/10.18419/opus-3733.

[19] Rodden, W. P., and Johnson, E. H., *MSC/NASTRAN Aeroelastic Analysis User's Guide*, 2nd ed., MSC, 1994.

[20] European Union Aviation Safety Agency, *Certification Specification and Acceptable Means of Compliance for Large Aeroplanes (CS-25)*, Amendment 27, 2023. URL https://www.easa.europa.eu/en/certification-specifications/cs-25-large-aeroplanes.

[21] Guyan, R. J., "Reduction of Stiffness and Mass Matrices," *AIAA Journal*, Vol. 3, No. 2, 1964. https://doi.org/10.2514/3.2874.

[22] Wright, J. R., and Cooper, J. E., *Introduction to Aircraft Aeroelasticity and Loads*, 2nd ed., Wiley, Chichester, UK, 2015. https://doi.org/10.1002/9781118700440.

[23] Albano, E., and Rodden, W. P., "A Doublet-Lattice Method for Calculating Lift Distributions on Oscillating Surfaces in Subsonic Flows," *AIAA Journal*, Vol. 7, No. 2, 1969. https://doi.org/10.2514/3.5086.

[24] Blair, M., "A Compilation of the Mathematics Leading to the Doublet Lattice Method," Technical Report, ADA256304, Air Force Wright Laboratory, 1992. URL https://apps.dtic.mil/sti/citations/ADA256304.

[25] Geißler, W., "Verfahren in der Instationären Aerodynamik," Technical Report, DLR-FB 93-21, German Aerospace Center (DLR), 1993. URL https://elib.dlr.de/37025/.

[26] Bisplinghoff, R. L., Ashley, H., and Halfman, R. L., *Aeroelasticity*, 2nd ed., Dover Publications Inc., Mineola, USA, 1983.

[27] Mauermann, T., "Flexible Aircraft Modelling for Flight Loads Analysis of Wake Vortex Encounters," Technical Report, DLR-FB 2010-37, German Aerospace Center (DLR), 2011. https://doi.org/10.24355/dbbs.084-201109120959-0.

[28] Beckert, A., and Wendland, H., "Multivariate Interpolation for Fluid-Structure-Interaction Problems Using Radial Basis Functions," *Aerospace Science and Technology*, Vol. 5, No. 2, 2001. https://doi.org/10.1016/S1270-9638(00)01087-7.

[29] Roger, K. L., "Airplane Math Modeling Methods For Active Control Design," *AGARD Conference Proceedings 228*, Advisory Group For Aerospace Research and Development of NATO (AGARD), 1977.

[30] Karpel, M., "Design for Active Flutter Suppression and Gust Alleviation Using State-Space Aeroelastic Modeling," *AIAA Journal*, Vol. 19, No. 3, 1982. https://doi.org/10.2514/3.57379.

[31] Tang, M., Böswald, M., Govers, Y., and Pusch, M., "Identification and Assessment of a Nonlinear Dynamic Actuator Model for Controlling an Experimental Flexible Wing," *CEAS Aeronautical Journal*, Vol. 12, 2021. https://doi.org/10.1007/s13272-021-00504-y.

[32] Fielding, C., and Flux, P. K., "Non-linearities in Flight Control Systems," *The Aeronautical Journal*, Vol. 107, 2003. https://doi.org/10.1017/S0001924000013543.

[33] Quero, D., Kaiser, C., Vuillemin, P., and Poussot-Vassal, C., "A State-Space Model for Loads Analysis Based on Tangential Interpolation," *International Forum on Aeroelasticity and Structural Dynamics (IFASD)*, Savannah, USA, 2019. URL https://elib.dlr.de/128079/.

[34] Antoulas, A. C., Lefteriu, S., and Ionita, A. C., "A Tutorial Introduction to the Loewner Framework for Model Reduction," *Model Reduction and Approximation*, edited by Peter Brenner et al., Society for Industrial and Applied Mathematics, Philadelphia, USA, 2017, Chap. 8, pp. 335–376. https://doi.org/10.1137/1.9781611974829.ch8.

[35] Mayo, A., and Antoulas, A. C., "A Framework for the Solution of the Generalized Realization Problem," *Linear Algebra and its Applications*, Vol. 425, 2007. https://doi.org/10.1016/j.laa.2007.03.008.

[36] Ionita, A. C., "Lagrange Rational Interpolation and its Applications to Approximation of Large-Scale Dynamical Systems," Ph.D. thesis, Rice University, Houston, USA, 2013. URL https://hdl.handle.net/1911/77180.

[37] Köhler, M., "On the Closest Stable Descriptor System in the Respective Spaces $RH_2$ and $RH_\infty$," *Linear Algebra and its Applications*, Vol. 443, 2014. https://doi.org/10.1016/j.laa.2013.11.012.

[38] Schulz, S., and Ossmann, D., "Estimation Of Global Structural Aircraft Loads Due To Atmospheric Disturbances For Structural Fatigue Estimation," *International Forum on Aeroelasticity and Structural Dynamics (IFASD)*, Madrid, Spain, 2022. URL https://elib.dlr.de/187735/.

[39] Reis, T., and Stykel, T., "Balanced Truncation Model Reduction of Second-Order Systems," *Mathematical and Computer Modelling of Dynamical Systems*, Vol. 14, No. 5, 2008. https://doi.org/10.1080/13873950701844170.

[40] Brenner, P., and Breiten, T., "Model Order Reduction Based on System Balancing," *Model Reduction and Approximation*, edited by Peter Brenner et al., Society for Industrial and Applied Mathematics, Philadelphia, USA, 2017, Chap. 8, pp. 261 – 295. https://doi.org/10.1137/1.9781611974829.ch6.

[41] Doyle, J. C., "Structured Uncertainty in Control System Design," *24th IEEE Conference on Decision and Control*, Fort Lauderdale, USA, 1985, pp. 260–265. https://doi.org/10.1109/CDC.1985.268842.

[42] Young, P. M., "Controller Design with Mixed Uncertainties," *Proceedings of the 1994 American Control Conference - ACC*, Vol. 2, Fort Lauderdale, USA, 1994, pp. 2333–2337. https://doi.org/10.1109/ACC.1994.752496.

[43] Young, P. M., "Controller Design with Real Parametric Uncertainty," *International Journal of Control*, Vol. 65, No. 3, 1996, pp. 469–509. https://doi.org/10.1080/00207179608921707.

[44] Bennani, S., Looye, G., and Mulder, J. A., "RCAM Design Challenge Presentation Document: the µ-Synthesis Approach," Technical report TP-088-11, GARTEUR, 1997.

[45] Doyle, J., "Analysis of Feedback Systems with Structured Uncertainties," *IEE Proceedings, Pt. D, Control Theory and Applications*, Vol. 129, No. 6, 1982. https://doi.org/10.1049/ip-d.1982.0053.

[46] Young, P. M., Newlin, M. P., and Doyle, J. C., "Practical Computation of the Mixed µ Problem," *1992 American Control Conference*, Chicago, USA, 1992, pp. 2190–2194. https://doi.org/10.23919/ACC.1992.4792521.

[47] Doyle, J. C., Glover, K., Khargonekar, P. P., and Francis, B. A., "State-space solutions to standard $H_2$ and $H_\infty$ control problems," *IEEE Transactions on Automatic Control*, Vol. 34, No. 8, 1989. https://doi.org/10.1109/9.29425.

[48] Seiler, P., Packard, A., and Gahinet, P., "An Introduction to Disk Margins [Lecture Notes]," *IEEE Control Systems Magazine*, Vol. 40, 2020. https://doi.org/10.1109/MCS.2020.3005277.

[49] German Aerospace Center (DLR), "oLAF - Evaluate the Potential of Active Load Alleviation for Efficient Long-Range Aircraft," [online resource], 2023. URL www.dlr.de/as/en/desktopdefault.aspx/tabid-17461/, [retrieved 20 November 2023].

[50] Schulze, M., Klimmek, T., Torrigiani, F., and Wunderlich, F. F., "Aeroelastic Design of the oLAF Reference Aircraft Configuration," *Deutscher Luft- und Raumfahrtkongress (DLRK)*, DGLR, Bremen, Germany, 2021. URL https://elib.dlr.de/143642/.

[51] Wunderlich, T. F., "Multidisciplinary Optimization of Flexible Wings with Manoeuvre Load Reduction for Highly Efficient Long-Haul Airliners," *Deutscher Luft- und Raumfahrtkongress (DLRK)*, DGLR, Dresden, Germany, 2022. https://doi.org/10.25967/570055.